Thickness of Lava Flows Within the Northern Smooth Plains on Mercury as Estimated by Partially Buried Craters

Jun Du, Mark Wieczorek, Wenzhe Fa

To cite this version:

Jun Du, Mark Wieczorek, Wenzhe Fa. Thickness of Lava Flows Within the Northern Smooth Plains on Mercury as Estimated by Partially Buried Craters. Geophysical Research Letters, 2020, 47 (20), 10.1029/2020GL090578 . hal-02980420

HAL Id: hal-02980420
https://hal.science/hal-02980420

Submitted on 27 Jan 2023

Geophysical Research Letters

RESEARCH LETTER

10.1029/2020GL090578

Thickness of Lava Flows Within the Northern Smooth Plains on Mercury as Estimated by Partially Buried Craters

Jun Du[1,2], **Mark A. Wieczorek**[2], **and Wenzhe Fa**[1,3,4]

[1]Institute of Remote Sensing and Geographical Information System, School of Earth and Space Sciences, Peking University, Beijing, China, [2]Laboratoire Lagrange, Université Côte d'Azur, Observatoire de la Côte d'Azur, CNRS, Nice, France, [3]State Key Laboratory of Lunar and Planetary Sciences, Macau University of Science and Technology, Macau, China, [4]CAS Center for Excellence in Comparative Planetology, Hefei, China

Key Points:

- Lava flow thicknesses on Mercury were estimated by modeling the topographic degradation of partially buried impact craters
- The median thickness of lava flows on Mercury is 228 m, which is greater than on the Moon by a factor of 2
- The reference topographic diffusivity on Mercury is 7.3 m^2/Myr, implying that topographic degradation is 3 times greater than on the Moon

Supporting Information:

- Supporting Information S1

Correspondence to:
J. Du,
jundu@pku.edu.cn

Citation:
Du, J., Wieczorek, M. A., & Fa, W. (2020). Thickness of lava flows within the northern smooth plains on Mercury as estimated by partially buried craters. *Geophysical Research Letters*, *47*, e2020GL090578. https://doi.org/10.1029/2020GL090578

Received 2 SEP 2020
Accepted 1 OCT 2020
Accepted article online 7 OCT 2020

Abstract Partially and completely buried impact craters are widely distributed over the northern smooth plains of Mercury. Using imagery data acquired from the MESSENGER mission, we compiled a database of 257 partially buried and 765 completely buried craters on Mercury. The elevation profiles of fresh craters were constructed, and by inputting these into a topographic degradation model, we estimated the lava flow thicknesses around partially buried craters. Along the edges of the northern smooth plains, lava flow thicknesses were inverted to be 23–536 m with a median of 228 m. Lava flow thicknesses on Mercury are twice that on the Moon, possibly due to a denser crust on Mercury that favors the ascent of magmas or to higher production rates of magmas. The topographic diffusivity used for crater degradation on Mercury is 3 times that for lunar craters, which is likely a result of a higher cratering rate on Mercury.

Plain Language Summary The thickness of lava flows is key to understanding volcanic processes on a planetary body. On Mercury, impact craters whose distal ejecta were subsequently flooded by lava flows are widely seen in the volcanic plains, providing a method to constrain lava flow thicknesses. For those craters whose entire rim is still visible, we estimated the regional lava flow thickness by modeling how the crater shape topographically degrades with time. Our results show that lava flows on Mercury are thicker than on the Moon, possibly because the magma can propagate upward more easily as a result of a denser crust, or perhaps because of higher internal magma production rates. Our findings also suggest that craters on Mercury degrade faster than on the Moon, which is most likely a result of a higher impact bombardment rate.

1. Introduction

Volcanic lava flows are widely seen on the surfaces of terrestrial planets and some of their moons, which can help to investigate the thermal evolution of the body. For the innermost planet Mercury, nearly one-fifth of its surface is believed to be volcanic in origin, which is attested by features such as volcanic vents, lava flow fronts, and partially and completely buried impact craters in the optical images acquired by the Mariner 10 and the MErcury Surface, Space ENvironment, GEochemistry, and Ranging (MESSENGER) missions (e.g., Denevi et al., 2013; Head et al., 2011). The most prominent volcanic units on Mercury are the large, contiguous smooth plains in the northern high latitudes that are characterized by low elevations and relatively fewer superposed craters with respect to the surrounding heavily cratered terrain (e.g., Denevi et al., 2013; Fa et al., 2016; Trask & Guest, 1975). In terms of composition, the lavas forming these volcanic plains are believed to be similar to low-iron, magnesian basalts and komatiites as inferred from the MESSENGER X-ray fluorescence data (e.g., Head et al., 2011; Nittler et al., 2011, 2020). The northern smooth plains may have formed from multiple eruptions, and the latest, most violent phase occurred 3.7 Ga, accounting for about 7% of the global surface area of the planet (Byrne et al., 2016; Denevi et al., 2013; Ostrach et al., 2015).

Impact craters that are completely buried by subsequent lava flows (i.e., ghost craters) often feature a circular wrinkle ridge over the crater rim (Watters et al., 2012), and they have been widely identified in the northern smooth plains. Estimates of their original rim heights from the rim height-diameter relation of fresh craters (Pike, 1988) can thus provide lower bounds for the lava flow thickness. Head et al. (2011) investigated the morphology and spatial distribution of 197 completely buried craters in the northern smooth plains using the MESSENGER/Mercury Dual Imaging System (MDIS) images. The presence of completely buried craters with diameters greater than 100 km indicates that lava flow thicknesses are at least 1–2 km. As more orbital images were acquired by the MESSENGER/MDIS camera, Ostrach et al. (2015) compiled a more complete database of craters whose rims are either completely or partially buried. Their documented craters have a diameter range of 25–157 km, and lava flow thicknesses were estimated to be greater than 0.7–1.8 km based on the rim height-crater diameter relation of fresh craters. However, the rim height-diameter relation used in both studies only applies to fresh craters, and the crater rim height could be overestimated due to topographic degradation during the period from crater formation to lava emplacement (Ostrach et al., 2015). Furthermore, this technique only provides lower limits rather than precise estimates of lava flow thicknesses, even if the crater degradation is neglected.

In a previous study of the Moon, we have shown that the mare basalt thicknesses can be estimated based on modeling the topographic degradation of partially buried craters (Du et al., 2019). Given that Mercury and the Moon share many commonalities in volcanic and crater degradation processes (e.g., Byrne, 2020; Fassett et al., 2017; Head et al., 2011), in this study, we use the same method and the MESSENGER imagery and altimetry data to estimate lava flow thicknesses on Mercury.

2. Data and Methods

2.1. Imagery and Topographic Data

The remote sensing data sets used in this study include optical images acquired by the MDIS camera and surface elevations measured by the Mercury Laser Altimeter (MLA), both onboard the MESSENGER spacecraft. The data sets include observations and measurements obtained during the last 2 years of the mission (released in 2017) that were hence not available for related previous studies (e.g., Fa et al., 2016; Fassett et al., 2017; Ostrach et al., 2015; Susorney et al., 2016). The imagery data are used to identify partially and completely buried craters and to study their crater morphology and geological settings. The topographic data are utilized to extract the elevation profiles of fresh craters for initial elevation profile modeling and the topographic profiles of partially buried craters for lava flow thickness estimation.

The final released MESSENGER/MDIS global mosaics were generated with a spatial resolution of 166 m/pixel, in comparison to those used by Ostrach et al. (2015) that had a spatial resolution of 400 m/pixel. In total, four global mosaics were produced with low, moderate, and high (east and west illuminations) incidence angles, which are favorable to highlight reflectance variations, surface morphological structures, and structures with large relief (Denevi et al., 2018; Herrick et al., 2018). Therefore, all four global mosaics are used in this study as they are complementary to each other.

The MLA has densely distributed laser footprints in the northern hemisphere where the spacecraft periapsis is low, which is favorable to study the topography of the northern smooth plains (Sun & Neumann, 2015; Zuber et al., 2012). The measured elevations along with the ancillary parameters were archived in the MLA Reduced Data Records (RDRs). The RDR data were interpolated by Neumann et al. (2016) to produce surface elevations in the Gridded Data Records (GDRs) format, and MDIS stereo images produced a complementary digital elevation model (DEM) (Becker et al., 2016). We compared the MLA RDR, MLA GDR, and MDIS DEM data sets and found that the MLA RDR data can reveal a more detailed representation of the surface topography (see Text S1). For this reason, we will use the MLA RDR as the topographic data in this study.

The MLA RDR data are archived in a tabular form, and for each elevation measurement, key parameters are recorded such as pulse number, channel ID, surface elevation, latitude, and longitude. The valid elevation measurements are assigned with channel IDs of 0, 1, 2, and 4, which have range biases of 3.57, 4.64, 16.04, and 52.91 m (Sun & Neumann, 2015). One transmitted pulse may provide multiple elevation measurements with different channel IDs, and we only used the record with the lowest channel ID that is the most accurate. Sometimes, even records with channel IDs of 0 and 1 are found to deviate from the surrounding elevations by over 500 m (Fassett et al., 2017), so we manually checked the extracted elevations and discarded any outliers. When producing the elevation profile, the crater center was identified by fitting a circle to three selected points along the crater rim. Here we used the MLA GDR data as the base map rather than the MDIS images, as there is a spatial misregistration as large as 5 km between the imagery and altimetry data due to different reference systems used (Stark et al., 2015). For a given crater, the study region is defined as a circle that extends three crater radii from the crater center. We azimuthally averaged the data as a function of distance from the crater center, excluding any atypical topographic features such as large craters and scarps (Du et al., 2019).

2.2. Partially and Completely Buried Craters

On Mercury, partially buried craters are those whose distal ejecta are mantled by lava flows whereas the crater rim and proximal ejecta are still protruding above the surrounding lavas. Based on this characteristic, two criteria are used to identify a partially buried crater: (1) the transition between crater ejecta and surrounding lava flows should be well defined as subsequent lava flows abruptly truncated the preexisting ejecta, and (2) the width of the exposed proximal ejecta should be narrower than the extent of the continuous ejecta for an unburied crater, which is about 0.8 times the crater radius (Gault et al., 1975). Figure 1a shows a typical partially buried crater ($D = 29.6$ km), where an abrupt boundary exists between the crater ejecta and nearby lava flows and the exposed ejecta width is only about 10–50% of the crater radius.

In some occasions, we also found craters where a part of their rims was breached by lava flows. An example crater ($D = 48.5$ km) of this type is shown in Figure 1b, for which the northern and western crater rims are exposed whereas the rest of the rim is buried by lava flows. This type of crater may have formed on a tilted surface or portions of its rim could have been destroyed by subsequent smaller craters, with lavas breaching the lowest part of the crater rim. The majority of the craters that formed prior to the emplacement of the smooth plains were completely buried by lava flows, and in Figure 1c, we show such a completely buried crater ($D = 43.1$ km). A wrinkle ridge is evident along the southern crater rim, which was formed by a compressional stress experienced by the thinnest lava (i.e., over the crater rim) due to the global contraction of the planet (Freed et al., 2012). For craters with rims partially or completely buried (as the two exemplary craters shown above), the initial crater rim height can be regarded as a lower limit of the lava flow thickness without considering crater rim erosion.

2.3. Shape Model of Fresh Craters

To simulate the topographic degradation of an impact crater, we started with the elevation profile of a fresh impact crater. We develop elevation profiles for fresh craters on Mercury by choosing those craters with sharp rims and well-preserved ejecta deposits as candidates (Susorney et al., 2016). We then limited the diameter range of the selected craters to 10–100 km, given that there are only a few craters larger than this range and they are all heavily modified and possess non-axisymmetric crater morphologies (Fassett et al., 2011). For craters smaller than 10 km, the fidelity of the elevation profile is insufficient due to the sparse distribution of the MLA measurements. As a result, the crater center is often missed, large gaps inhibit the azimuthal averaging, and the crater center is difficult to determine from the MLA GDR (Susorney et al., 2016). For craters of 10–100 km in size, we found that the overall shape changes smoothly with diameter. A crater was then classified either as a transitional or complex crater based on whether a central peak is present, while simple craters have diameters less than the lower limit investigated in this study. The smallest crater with a central peak was found to be 24.7 km in diameter, which was used as the boundary to separate the two diameter regimes. As there is no significant difference in morphology between craters in the northern smooth plains and the heavily cratered terrain (Barnouin et al., 2012; Susorney et al., 2016), we did not distinguish between the two in this study. In total, we used 36 fresh craters to model the initial topographic profiles (Text S2), and as a result, two types of initial elevation profiles were established for transitional ($10 < D < 25$ km) and complex ($25 \leqslant D < 100$ km) craters (see Table S2 and Figure S2).

2.4. Lava Flow Thickness Estimation Method

The topographic degradation of impact craters on Mercury can be modeled as a diffusive process, where micrometeoroid bombardment is believed to be the major process that erodes a crater (Fassett et al., 2017). Each given initial elevation profile was input into a diffusion equation to model the topographic degradation as a function of time. For partially buried craters, the final modeled profile is dependent on six parameters, including the initial crater diameter, exterior and interior lava flow thicknesses, and two diffusivity-time products before and after the lava flow emplacement (Du et al., 2019). By varying the parameters in the model space, the best fitting lava flow thickness is determined by the minimum misfit between the final modeled and observed topographic profiles. As a by-product, if the age of the smooth plains is known a priori, the best fitting topographic diffusivity can also be determined (Du et al., 2019). The detailed parameterization and model setup are given in the supporting information, followed by the uncertainty calculation of the model parameter that considers the uncertainty of the initial elevation profile and the standard error of the

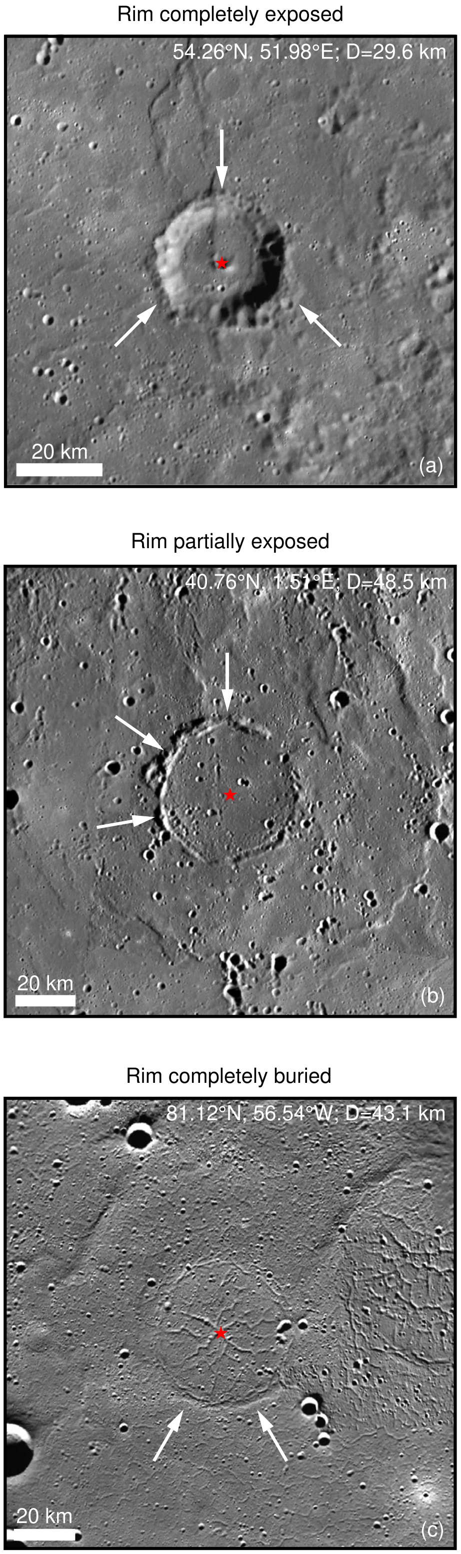

Figure 1. MDIS images of three unnamed impact craters whose rim is (a) completely exposed ($D = 29.6$ km), (b) partially exposed ($D = 48.5$ km), and (c) completely buried ($D = 43.1$ km). The red stars show the locations of crater centers, and the white arrows point to the exposed ejecta boundaries in (a) and (b) and the wrinkle ridge in (c).

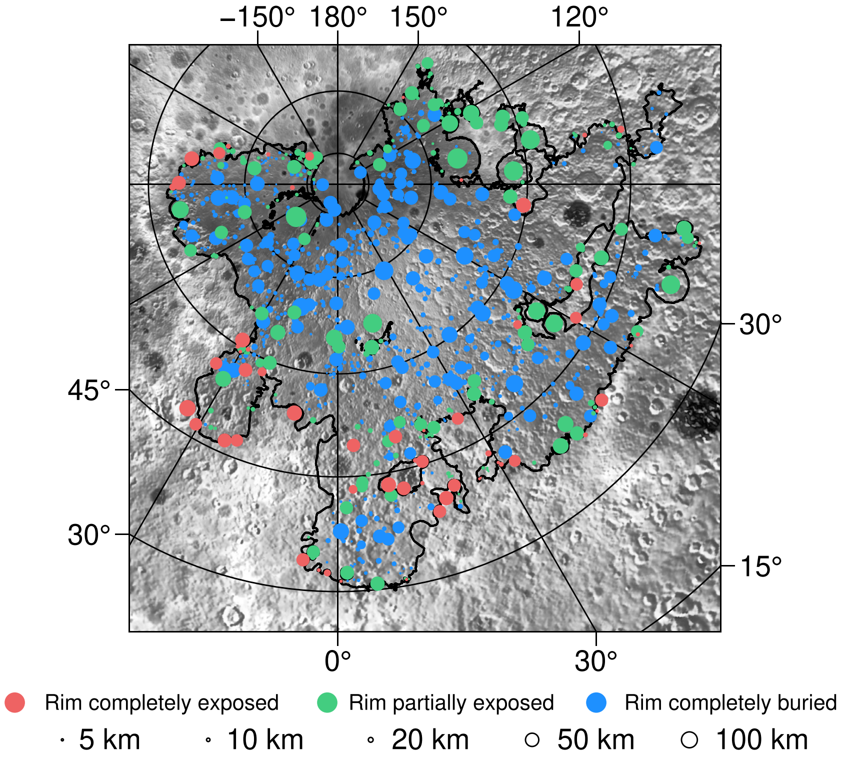

Figure 2. Distribution of craters with rims completely exposed (red, $N = 59$), rims partially exposed (green, $N = 198$), and rims completely buried (blue, $N = 765$). The smooth plains boundaries (black) is taken from Denevi et al. (2013), and the base map is a shaded-relief map derived from the MDIS DEM. The size of the circles increases with crater diameter.

observed elevation profile (Text S3). Complementary to this work, we also present lower bounds for lava flow thicknesses based on the rim heights of impact craters whose rims are either partially or completely buried. The rim heights were obtained based on the rim height-crater diameter relation derived for fresh craters (Figure S2a).

3. Lava Flow Thicknesses

Using the Crater Helper Tools extension (Nava, 2011) on the ArcGIS platform, we established a database of buried impact craters within the northern smooth plains of Mercury from the MESSENGER/MDIS global mosaics. The crater coordinates and diameters were determined by fitting a circle to three selected points along either the exposed crater rim or the wrinkle ridge over the buried crater rim. We further defined a rim exposure parameter as the length of the exposed rim divided by the rim circumference. Each of our identified partially buried craters has a rim exposure of 10–100%, as craters with a shorter segment of exposed rim are problematic in determining the crater diameter. The same rule applies to our identified completely buried craters, where a wrinkle ridge with a length of 10% of the rim circumference at least should be visible. In total, we identified 765 completely buried craters and 257 partially buried craters, of which 59 have their rims completely exposed (Table S1). The crater diameters span from 3 to 323 km, with a median of 13 km (see Text S4). The spatial distribution of partially and completely buried craters is shown in Figure 2. Partially buried craters are found to occur preferentially along the smooth plains/cratered terrain boundaries, most likely because the lava flows at the edges of the smooth plains are thinner than the interior. Completely buried craters are much more abundant and are distributed more uniformly within the smooth plains. Several isolated regions were found with sparsely distributed buried craters (e.g., near crater Rustaveli at 52°N, 83°E), which are most likely due to burial by subsequent basin/crater ejecta or to the poor illumination conditions of the optical images that inhibited the crater identification.

Ostrach et al. (2015) also constructed a database for buried impact craters with diameters of 8–678 km, and here we use the cumulative number of craters larger than diameter D per km^2 for comparing the two

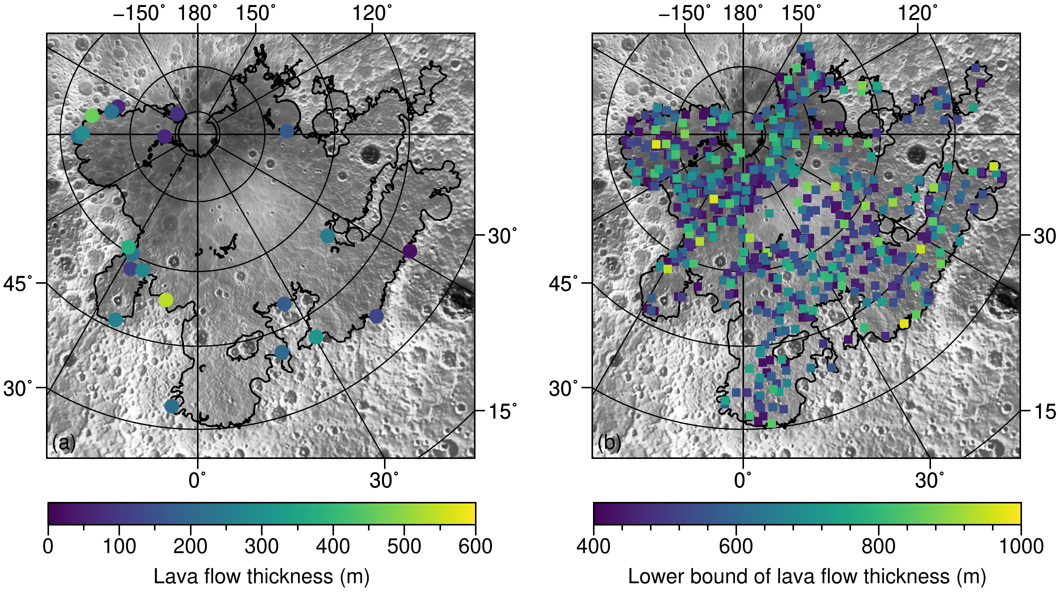

Figure 3. (a) Lava flow thicknesses estimated from partially buried craters with fully exposed rims. (b) Lower bounds of lava flow thicknesses obtained from craters with partially or completely buried rims assuming no crater degradation. The black lines represent the boundaries of the northern smooth plains (Denevi et al., 2013).

databases (Figure S4). Overall, we found more craters within the 3–64 km range but fewer between 64 and 678 km. As an example, Ostrach et al. (2015) stated that their crater database is complete for craters larger than 32 km, but we found a cumulative number of craters greater than 32 km that is 42% larger than their value. Within the range of 3–64 km, our crater database is more complete as (1) we identified partially buried craters with rim exposures of 10–100%, whereas Ostrach et al. (2015) only recorded those with rim exposures ⩽25%; (2) we used images with a better spatial resolution acquired during the last phase of the mission; and (3) we used images with different viewing geometries that favor the recognition of buried craters (Herrick et al., 2018). For craters larger than 64 km, our cumulative number is smaller because we used a more conservative approach (e.g., a clear rim exposure >10%) to identify candidate craters that are usually heavily modified (Fassett et al., 2011). As an example, a 678-km-diameter basin (70°N, 80°W) was identified by Ostrach et al. (2015), whereas we did not include it in our database as most of its rim is either destructed or buried and thus is hardly discernible.

To obtain robust estimates of lava flow thicknesses, we started with 53 craters 10–83 km in diameter with fully exposed rims. We then discarded craters with complex geological settings such as those formed on basin/crater rims, wrinkles ridges, and a tilted background. Next, considering the fidelity of the extracted elevation profile, we further removed craters without any elevation measurement within half of the crater radius from the crater center (roughly equal to the floor radius of the crater). We also excluded craters that have an atypically high misfit (larger than 100 m) between the extracted profile and the best fit of the modeled profile and those craters whose lava flow thicknesses were found to be 0 km (within uncertainties). In the end, 21 craters were kept that were suitable for further analyses. The selected craters are concentrated along the edges of the northern smooth plains with diameters of 11 to 83 km as shown in Figure 3a.

The obtained lava flow thicknesses range from 23 to 536 m with a median value of 228 m (see Table S5), and there is no clear pattern in their spatial distribution (Figure 3a), nor any correlation with the gravity and geochemical data (e.g., Mazarico et al., 2018; Nittler et al., 2020). The average uncertainty of the estimated lava flow thicknesses is 91 m. All 21 craters were found to have lavas in their interiors, with an average thickness of 1,138 m. This is because impact cratering events may create stress conditions that focus the ascent of magmas into the crater interior (Michaut & Pinel, 2018). If crater degradation was not considered, the lava flow thicknesses would be substantially larger, ranging from 135 to 608 m with a median value of 346 m. By neglecting crater degradation, the lava flow thickness would be overestimated by nearly 50% in terms of the median value (see Text S5).

We also made use of craters where the rim was either entirely or partially buried by lava flows to provide lower bounds for lava flow thicknesses in the interior of the northern smooth plains (Figure 3b). We used 585 craters with diameters of 10–93 km. The initial crater rim heights range from 411 to 979 m with a median of 538 m, which can serve as lower limits for lava flow thicknesses. However, these are very loose constraints as crater degradation could have taken place before lava emplacement, which would act to decrease the lava flow thicknesses. We attempted to estimate the rim height reduction from crater formation, but there are many uncertainties, such as when the crater formed and how the topographic diffusivity varied with time. The spatial distribution of the thickness estimates shown in Figure 3b does not show any systematic trends. We note that the depth of large ghost basins observed in gravity anomaly maps shows that lava infillings in the center could be several kilometers thick in places (Deng et al., 2018).

4. Total Volume of Lava Flows

Using a median thickness of 228 m obtained from partially buried craters with fully exposed rims, along with a surface area of 5.4×10^6 km^2 (Denevi et al., 2013), the total volume of lava flows within the northern smooth plains is estimated to be 1.2×10^6 km^3. This value, however, only represents a lower bound, as we were not able to estimate the total thickness in the center of the plains through partially buried craters. If the lower limits of lava flow thicknesses (0.4–1.0 km) obtained from craters with completely or partially buried rims are used, the total volume would increase by a factor of 2–5 to $2.2–5.4 \times 10^6$ km^3. It is noteworthy that, in addition to the large contiguous northern smooth plains, small patchy smooth plains of volcanic origin are also widely distributed over the planet, which were dated to be 3.5 to 3.8 Gyr old (Byrne et al., 2016). These deposits cover 11% surface area of the planet, in comparison to the 7% of the northern smooth plains (Denevi et al., 2013). The basalt thickness (200–400 m) in the isolated mare deposits on the lunar farside is about half of the total basalt thickness (740 m) in the nearside mare plains (Gong et al., 2016; Yingst & Head, 1997). Given their smaller area extents, it is therefore expected that on Mercury, the small patchy smooth plains may also have smaller lava flow thicknesses and volumes as compared with the northern smooth plains. Given that the average thickness of the crust is believed to be about 12–30 km (Padovan et al., 2017; Tosi et al., 2013), our result also suggests that the uppermost smooth plains account for only a small portion of the magmatic materials emplaced on Mercury after curst formation (Klima et al., 2018; Vander Kaaden & McCubbin, 2015).

Similar to the northern smooth plains on Mercury, the lunar surface is also covered by lava flows, and their thicknesses have been estimated from partially buried craters (Du et al., 2019). A comparison of lava flow volumes between the two bodies provides insights into the mechanisms of the production and eruption of magmas. For the lunar data, we first consider only those partially buried craters that formed on the highland crust before mare flooding (usually identified along the mare margins as well), which give the total thickness of lavas in the vicinity of the crater. The median lava flow thickness on the Moon was estimated to be 105 m using 27 craters of this type (Du et al., 2019), which is about half of what we found on Mercury. Both the Moon and Mercury have a substantial number of craters whose rims are either completely or partially buried by lava flows. These craters provide lower bounds on the median thicknesses of 538 m for Mercury and 304 m for the Moon. Lastly, we noted that large buried impact basins have been detected using gravity data in both the northern smooth plains of Mercury and the mare of the Moon and that estimates of their initial depths can constrain the overall lava flow thickness. On Mercury, local lenses of lava flows in ghost basins were found to be at least 6.5–10.6 km thick (Deng et al., 2018), whereas on the Moon, the thickness of mare basalts infilling ghost basins was estimated to be at least 1.5–7 km (Evans et al., 2016). All evidence suggests that lava flows on Mercury are thicker than on the Moon, both along their edges of the flooded plains and within their interiors.

Given that the surface area of northern smooth plains on Mercury is about that of lunar maria (Head, 1975), the total volume of lava flows on Mercury is about 2 times larger than on the Moon. One potential explanation for this difference could be a result of differing density contrasts between the magmas and crust for the two bodies. Lunar magmas are thought to be negatively buoyant in the crust, given a magma density of 2,980–3,240 kg/m^3 and a crustal density of 2,200–2,870 kg/m^3 (Huang & Wieczorek, 2012; Kiefer et al., 2012; Wilson & Head, 2017). For Mercury, however, magmas are expected to be always buoyant, as molten magmas

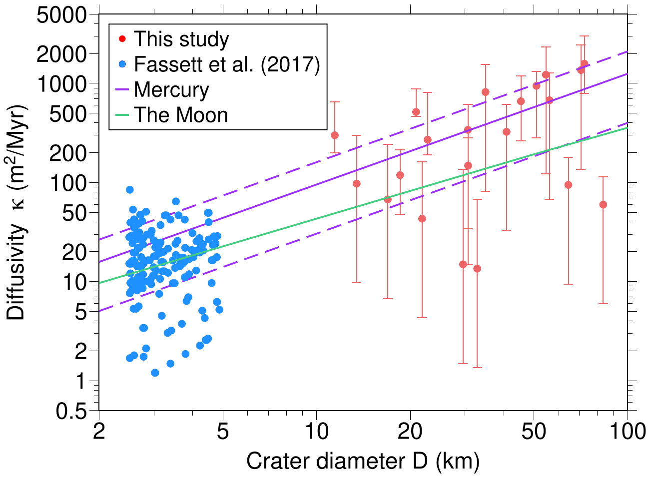

Figure 4. Estimated topographic diffusivity for craters on Mercury as a function of crater diameter (red dots). Estimates from Fassett et al. (2017) are plotted as blue dots, and the best fitting diffusivity-diameter relation for both studies ($\kappa_{\text{Mercury}} = 7.3 \times D^{1.12}$) is shown by the purple solid line with one-sigma uncertainties as dashed lines. The diameter dependence of the topographic diffusivity for lunar craters ($\kappa_{\text{Moon}} = 5.1 \times D^{0.93}$) (green) is shown for reference (Du et al., 2019).

likely intruded a crust of a similar composition (Klima et al., 2018; Vander Kaaden & McCubbin, 2015). As a result, magmas on Mercury should reach the surface more easily. An alternative explanation for the greater volume of lavas on Mercury is that the magma production rates were greater in the interior of Mercury in comparison to the Moon (Laneuville et al., 2013; Padovan et al., 2017; Tosi et al., 2013).

5. Size Dependence of Topographic Diffusivity

One parameter of the crater degradation model that is well constrained is the topographic diffusivity times the duration since lava flooding. The best fitting topographic diffusivity can thus be obtained by dividing this product by the age of the northern smooth plains (Table S6), which is estimated to be 3.7 ± 0.01 Gyr (Byrne et al., 2016; Ostrach et al., 2015). As is shown in Figure 4, our estimates show that the topographic diffusivity increases with crater diameter, indicating that the topographic degradation of craters on Mercury is scale dependent. In this figure, we also plot the topographic diffusivities estimated from a group of 204 small craters ($D = 2$–5 km) by Fassett et al. (2017), which shows a positive correlation with crater diameter as well.

Though there is much scatter, the diffusivity-diameter relation of both data sets combined can be fitted by a power law ($\kappa = \kappa_0 \times D^{\beta}$), which is characterized by a reference diffusivity at 1-km diameter (κ_0) and an exponent (β). For reference, we also plot in this figure the diameter dependence of the topographic diffusivity for lunar craters obtained from Du et al. (2019). This shows that the diameter dependence of the diffusivity is broadly similar, but the absolute diffusivity is about 3 times greater on Mercury than on the Moon. More specifically, the reference diffusivity and the exponent factor of craters on Mercury are greater than those of lunar craters by about 40% and 20%, respectively. Fassett et al. (2017) and Fassett and Thomson (2014) came to a similar conclusion using craters on the Moon and Mercury in the 2.5–5 km diameter range.

As most crater topographic degradation is considered to be a result of meteoroid bombardment (e.g., Culling, 1960; Soderblom, 1970), the topographic diffusivity is closely related to the impact cratering rate. Therefore, a comparison of topographic diffusivity on Mercury and the Moon could shed light on the impact cratering history in the inner solar system. To address this issue, Le Feuvre and Wieczorek (2011) modeled the impact cratering rates on the two bodies based on orbital dynamics, and their result showed that the impact cratering rate on Mercury should be nearly 3 times that as on the Moon. Surface roughness and regolith thickness on Mercury are also greater than on the Moon by roughly a factor of 3, which were similarly interpreted to be a result of a higher impact cratering rate on Mercury (Fa et al., 2016; Kreslavsky & Head, 2015; Kreslavsky et al., 2014). Therefore, it can be expected that the impact cratering rate on Mercury should be 3 times greater than on the Moon, which is consistent with our topographic diffusivity results on the two bodies.

We noted several factors that could complicate our estimated topographic diffusivities. First, the initial crater profile could vary from place to place due to specific impact conditions. Second, the diffusion equation used in this study was constructed in an idealized axisymmetric scenario, whereas the actual topographic degradation could be more azimuthally heterogenous. Third, the absolute age of the northern smooth plains is uncertain. As an example, if the age of this surface was estimated using impact cratering scaling laws for non-porous targets (as opposed to porous targets as is commonly used), the age of the northern smooth plains could be as young as 2 Gyr (Le Feuvre & Wieczorek, 2011; Ostrach et al., 2015). Nevertheless, this change in age would not change the overall finding that the topographic diffusivity on Mercury is larger than on the Moon.

6. Conclusions

Imagery data from the MESSENGER mission were used to construct a database of craters in the northern smooth plains that were either partially or completely buried by lava flows. Lava flow thicknesses were estimated for 21 craters whose rims are fully exposed, showing that the lava flow thicknesses vary from 23 to

536 m with a median of 228 m. These craters, however, are primarily located along the plains/highlands boundaries, and in the center of the plains, lava flow thicknesses were estimated to be at least 411–979 m based on estimated rim heights of completely buried craters. The median thickness of lava flows within the northern smooth plains on Mercury was found to be larger than that within the lunar maria by a factor of 2, and we interpreted this as a result of magmas being either more buoyant within the crust of Mercury than on the Moon, or to higher magma production rates on Mercury than the Moon. We also found that the topographic diffusivity of craters on Mercury increases with crater diameter and that our obtained topographic diffusivity is about 3 times greater than that of lunar craters, possibly due to a higher impact cratering rate on the planet.

Data Availability Statement

According to the FAIR Data principles, the authors declare the following Data Availability Statement: the MESSENGER MDIS imagery data and MLA RDR altimetry data are available at the NASA PDS Geosciences Node (https://pds-geosciences.wustl.edu/missions/messenger/index.htm). Anyone can download the data for free and without any licenses. The database of partially and completely buried craters is provided online (https://zenodo.org/record/4052846#.X3BZmS1h1hE).

Acknowledgments

We thank G. A. Neumann for instructions on the MLA data format. We also thank H. C. M. Susorney and J. L. Whitten for their helpful comments to improve the quality of this paper. This work was funded jointly by the B-type Strategic Priority Program of the Chinese Academy of Sciences (XDB41000000), the National Natural Science Foundation of China (41941002, 11573005), the Science and Technology Development Fund of Macau (043/2016/A2), the French Space Agency (CNES), and the China Scholarship Council doctoral fellowship (201606010077). Figures were created by the Generic Mapping Tools (Wessel & Smith, 1991). This is PKU PRSL contribution 14.

References

Barnouin, O. S., Zuber, M. T., Smith, D. E., Neumann, G. A., Herrick, R. R., Chappelow, J. E., & Prockter, L. M. (2012). The morphology of craters on Mercury: Results from MESSENGER flybys. *Icarus*, *219*(1), 414–427. https://doi.org/10.1016/j.icarus.2012.02.029

Becker, K., Robinson, M., Becker, T., Weller, L., Edmundson, K., Neumann, G., & Solomon, S. (2016). First global digital elevation model of Mercury. In *47th Lunar and Planetary Science Conference*, #2959.

Byrne, P. K. (2020). A comparison of inner solar system volcanism. *Nature Astronomy*, *4*, 321–327. https://doi.org/10.1038/s41550-019-0944-3

Byrne, P. K., Ostrach, L. R., Fassett, C. I., Chapman, C. R., Denevi, B. W., Evans, A. J., & Solomon, S. C. (2016). Widespread effusive volcanism on Mercury likely ended by about 3.5 Ga. *Geophysical Research Letters*, *43*, 7408–7416. https://doi.org/10.1002/2016GL069412

Culling, W. E. H. (1960). Analytical theory of erosion. *Journal of Geology*, *68*(3), 336–344. https://doi.org/10.1086/626663

Denevi, B. W., Chabot, N. L., Murchie, S. L., Becker, K. J., Blewett, D. T., Domingue, D. L., et al. (2018). Calibration, projection, and final image products of MESSENGER's Mercury Dual Imaging System. *Space Science Reviews*, *214*(2), 52. https://doi.org/10.1007/s11214-017-0440-y

Denevi, B. W., Ernst, C. M., Meyer, H. M., Robinson, M. S., Murchie, S. L., Whitten, J. L., et al. (2013). The distribution and origin of smooth plains on Mercury. *Journal of Geophysical Research: Planets*, *118*, 891–907. https://doi.org/10.1002/jgre.20075

Deng, Q., Li, F., Yan, J., Xiao, Z., & Rodriguez, J. A. P. (2018). Buried impact features on Mercury as revealed by gravity data. *Journal of Geophysical Research: Planets*, *123*, 3005–3019. https://doi.org/10.1029/2018JE005801

Du, J., Fa, W., Wieczorek, M. A., Xie, M., Cai, Y., & Zhu, M. H. (2019). Thickness of lunar mare basalts: New results based on modeling the degradation of partially buried craters. *Journal of Geophysical Research: Planets*, *124*, 2430–2459. https://doi.org/10.1029/2018JE005872

Evans, A. J., Soderblom, J. M., Andrews-Hanna, J. C., Solomon, S. C., & Zuber, M. T. (2016). Identification of buried lunar impact craters from GRAIL data and implications for the nearside maria. *Geophysical Research Letters*, *43*, 2445–2455. https://doi.org/10.1002/2015GL067394

Fa, W., Cai, Y., Xiao, Z., & Tian, W. (2016). Topographic roughness of the northern high latitudes of Mercury from MESSENGER Laser Altimeter data. *Geophysical Research Letters*, *43*, 3078–3087. https://doi.org/10.1002/2016GL068120

Fassett, C. I., Crowley, M. C., Leight, C., Dyar, M. D., Minton, D. A., Hirabayashi, M., & Watters, W. A. (2017). Evidence for rapid topographic evolution and crater degradation on Mercury from simple crater morphometry. *Geophysical Research Letters*, *44*, 5326–5335. https://doi.org/10.1002/2017GL073769

Fassett, C. I., Kadish, S. J., Head, J. W., Solomon, S. C., & Strom, R. G. (2011). The global population of large craters on Mercury and comparison with the Moon. *Geophysical Research Letters*, *38*, L10202. https://doi.org/10.1029/2011GL047294

Fassett, C. I., & Thomson, B. J. (2014). Crater degradation on the lunar maria: Topographic diffusion and the rate of erosion on the Moon. *Journal of Geophysical Research: Planets*, *119*, 2255–2271. https://doi.org/10.1002/2014JE004698

Freed, A. M., Blair, D. M., Watters, T. R., Klimczak, C., Byrne, P. K., Solomon, S. C., & Melosh, H. J. (2012). On the origin of graben and ridges within and near volcanically buried craters and basins in Mercury's northern plains. *Journal of Geophysical Research*, *117*, E00L06. https://doi.org/10.1029/2012JE004119

Gault, D. E., Guest, J. E., Murray, J. B., Dzurisin, D., & Malin, M. C. (1975). Some comparisons of impact craters on Mercury and the Moon. *Journal of Geophysical Research*, *80*(17), 2444–2460. https://doi.org/10.1029/JB080i017p02444

Gong, S., Wieczorek, M. A., Nimmo, F., Kiefer, W. S., Head, J. W., Huang, C., et al. (2016). Thicknesses of mare basalts on the Moon from gravity and topography. *Journal of Geophysical Research: Planets*, *121*, 854–870. https://doi.org/10.1002/2016JE005008

Head, J. W. (1975). Lunar mare deposits: Areas, volumes, sequence, and implication for melting in source areas. In *Conference on Origins of Mare Basalts and Their Implications for Lunar Evolution* (pp. 66–69).

Head, J. W., Chapman, C. R., Strom, R. G., Fassett, C. I., Denevi, B. W., Blewett, D. T., et al. (2011). Flood volcanism in the northern high latitudes of Mercury revealed by MESSENGER. *Science*, *333*(6051), 1853–1856. https://doi.org/10.1126/science.1211997

Herrick, R. R., Bateman, E. M., Crumpacker, W. G., & Bates, D. (2018). Observations from a global database of impact craters on Mercury with diameters greater than 5 km. *Journal of Geophysical Research: Planets*, *123*, 2089–2109. https://doi.org/10.1029/2017JE005516

Huang, Q., & Wieczorek, M. A. (2012). Density and porosity of the lunar crust from gravity and topography. *Journal of Geophysical Research*, *117*, E05003. https://doi.org/10.1029/2012JE004062

Kiefer, W. S., Macke, R. J., Britt, D. T., Irving, A. J., & Consolmagno, G. J. (2012). The density and porosity of lunar rocks. *Geophysical Research Letters*, *39*, L07201. https://doi.org/10.1029/2012GL051319

Klima, R. L., Denevi, B. W., Ernst, C. M., Murchie, S. L., & Peplowski, P. N. (2018). Global distribution and spectral properties of low-reflectance material on Mercury. *Geophysical Research Letters*, *45*, 2945–2953. https://doi.org/10.1002/2018GL077544

Kreslavsky, M. A., & Head, J. W. (2015). A thicker regolith on Mercury. In *46th Lunar and Planetary Science Conference*, #1246.

Kreslavsky, M. A., Head, J. W., Neumann, G. A., Zuber, M. T., & Smith, D. E. (2014). Kilometer-scale topographic roughness of Mercury: Correlation with geologic features and units. *Geophysical Research Letters*, *41*, 8245–8251. https://doi.org/10.1002/2014GL062162

Laneuville, M., Wieczorek, M. A., Breuer, D., & Tosi, N. (2013). Asymmetric thermal evolution of the Moon. *Journal of Geophysical Research: Planets*, *118*, 1435–1452. https://doi.org/10.1002/jgre.20103

Le Feuvre, M., & Wieczorek, M. A. (2011). Nonuniform cratering of the Moon and a revised crater chronology of the inner solar system. *Icarus*, *214*(1), 1–20. https://doi.org/10.1016/j.icarus.2011.03.010

Mazarico, E., Genova, A., Goossens, S., Neumann, G., Smith, D., & Zuber, M. (2018). The crust of Mercury after the MESSENGER gravity investigation. In *Mercury: Current and Future Science of the Innermost Planet*.

Michaut, C., & Pinel, V. (2018). Magma ascent and eruption triggered by cratering on the Moon. *Geophysical Research Letters*, *45*, 6408–6416. https://doi.org/10.1029/2018GL078150

Nava, R. A. (2011). *Crater Helper Tools for ArcGIS 10.0*. Flagstaff: U.S. Geological Survey. (U.S. Geological Survey Reference Manual).

Neumann, G. A., Perry, M. E., Mazarico, E., Ernst, C. M., Zuber, M. T., Smith, D. E., & Solomon, S. C. (2016). Mercury shape model from laser altimetry and planetary comparisons. In *47th Lunar and Planetary Science Conference*, #2087.

Nittler, L. R., Frank, E. A., Weider, S. Z., Crapster-Pregont, E., Vorburger, A., Starr, R. D., & Solomon, S. C. (2020). Global major-element maps of Mercury from four years of MESSENGER X-Ray Spectrometer observations. *Icarus*, *345*, 113716. https://doi.org/10.1016/j.icarus.2020.113716

Nittler, L. R., Starr, R. D., Weider, S. Z., McCoy, T. J., Boynton, W. V., Ebel, D. S., et al. (2011). The major-element composition of Mercury's surface from MESSENGER X-ray spectrometry. *Science*, *333*(6051), 1847–1850. https://doi.org/10.1126/science.1211567

Ostrach, L. R., Robinson, M. S., Whitten, J. L., Fassett, C. I., Strom, R. G., Head, J. W., & Solomon, S. C. (2015). Extent, age, and resurfacing history of the northern smooth plains on Mercury from MESSENGER observations. *Icarus*, *250*, 602–622. https://doi.org/10.1016/j.icarus.2014.11.010

Padovan, S., Tosi, N., Plesa, A. C., & Ruedas, T. (2017). Impact-induced changes in source depth and volume of magmatism on Mercury and their observational signatures. *Nature Communications*, *8*, 1945. https://doi.org/10.1038/s41467-017-01692-0

Pike, R. J. (1988). Geomorphology of impact craters on Mercury. In F. Vilas, C. R. Chapman, M. S. Matthews (Eds.), *Mercury* (pp. 165–273). Tucson: University of Arizona Press.

Soderblom, L. A. (1970). A model for small-impact erosion applied to the lunar surface. *Journal of Geophysical Research*, *75*(14), 2655–2661. https://doi.org/10.1029/JB075i014p02655

Stark, A., Oberst, J., Preusker, F., Gwinner, K., Peale, S. J., Margot, J. L., & Solomon, S. C. (2015). Mercury's rotational parameters from MESSENGER image and laser altimeter data: A feasibility study. *Planetary and Space Science*, *117*, 64–72. https://doi.org/10.1016/j.pss.2015.05.006

Sun, X., & Neumann, G. A. (2015). Calibration of the Mercury Laser Altimeter on the MESSENGER Spacecraft. *IEEE Transactions on Geoscience and Remote Sensing*, *53*(5), 2860–2874. https://doi.org/10.1109/TGRS.2014.2366080

Susorney, H. C. M., Barnouin, O. S., Ernst, C. M., & Johnson, C. L. (2016). Morphometry of impact craters on Mercury from MESSENGER altimetry and imaging. *Icarus*, *271*, 180–193. https://doi.org/10.1016/j.icarus.2016.01.022

Tosi, N., Grott, M., Plesa, A. C., & Breuer, D. (2013). Thermochemical evolution of Mercury's interior. *Journal of Geophysical Research: Planets*, *118*, 2474–2487. https://doi.org/10.1002/jgre.20168

Trask, N. J., & Guest, J. E. (1975). Preliminary geologic terrain map of Mercury. *Journal of Geophysical Research*, *80*(17), 2461–2477. https://doi.org/10.1029/JB080i017p02461

Vander Kaaden, K. E., & McCubbin, F. M. (2015). Exotic crust formation on Mercury: Consequences of a shallow, FeO-poor mantle. *Journal of Geophysical Research: Planets*, *120*, 195–209. https://doi.org/10.1002/2014JE004733

Watters, T. R., Solomon, S. C., Klimczak, C., Freed, A. M., Head, J. W., Ernst, C. M., & Byrne, P. K. (2012). Extension and contraction within volcanically buried impact craters and basins on Mercury. *Geology*, *40*(12), 1123–1126. https://doi.org/10.1130/G33725.1

Wessel, P., & Smith, W. H. F. (1991). Free software helps map and display data. *EOS Transactions American Geophysical Union*, *72*(41), 441–446. https://doi.org/10.1029/90EO00319

Wilson, L., & Head, J. W. (2017). Generation, ascent and eruption of magma on the Moon: New insights into source depths, magma supply, intrusions and effusive/explosive eruptions (Part 1: Theory). *Icarus*, *283*, 146–175. https://doi.org/10.1016/j.icarus.2016.05.031

Yingst, R. A., & Head, J. W. (1997). Volumes of lunar lava ponds in South Pole-Aitken and Orientale basins: Implications for eruption conditions, transport mechanisms, and magma source regions. *Journal of Geophysical Research*, *102*, 10,909–10,931. https://doi.org/10.1029/97JE00717

Zuber, M. T., Smith, D. E., Phillips, R. J., Solomon, S. C., Neumann, G. A., Hauck, S. A., et al. (2012). Topography of the northern hemisphere of Mercury from MESSENGER laser altimetry. *Science*, *336*(13), 217–220. https://doi.org/10.1126/science.1218805